Int. J. Electrochem. Sci., 16 **(2021)** Article Number: 211059, doi: 10.20964/2021.10.07

International Journal of
ELECTROCHEMICAL
SCIENCE
www.electrochemsci.org

Controllable synthesis and electrochemical performance of Fe_2O_3@ graphene foam composite as anode materials for sodium-ion batteries

Wang Lianyang[1], *Yinling Zhang*[3], *Li Dongping*[2], *Wang Xin*[2,*], *Li Xingyi*[1,*]

[1] School of Materials Science and Engineering, Jiamusi University, Jiamusi 154007, PR China
[2] School of Materials Science and Chemical Engineering, Harbin University of Science and Technology, Harbin 150080, PR China
[3] Heilongjiang Academy of Mechanical Science, Harbin 150080, PR China
*E-mail: wanglianyangcl2017@163.com, 672346534@qq.com

Received: 28 April 2021 / *Accepted:* 12 July 2021 / *Published:* 10 September 2021

We designed and synthesized a new self-supporting composite with Fe_2O_3 nanorods and three-dimensional graphene foam (GF). Fe_2O_3 tightly combined with graphene foam can well maintain the microstructure of the electrode, and can effectively reduce the volume expansion problem and improve the cycle stability of the electrode. Graphene foam as a matrix material effectively improves the conductivity of the electrode material, providing a channel for rapid electron transfer. Fe_2O_3@GF shows better lithium storage performance than electrode materials calcined at 300℃ and 500℃, and Fe_2O_3-400@GF calcined at 400℃ shows good cycle stability and high-rate performance, with a retention capacity of 410 $mAh \cdot g^{-1}$at 2 $A \cdot g^{-1}$.

Keywords: Fe_2O_3; Graphene foam; Anode material; Electrochemical performance; Sodium-ion batteries

1. INTRODUCTION

In recent decades, rechargeable lithium-ion batteries have been widely used as power sources for various portable electronic devices and electric vehicles [1-3]. However, due to the exponential increase in the consumption of lithium resources, lithium is no longer suitable for large-scale energy storage [4-6]. In contrast to lithium-ion batteries, sodium-ion batteries have attracted increasing attention in the field of large-scale energy storage and low-speed electric vehicles due to their low cost and abundant reserves [7-10]. Sodium-ion batteries are expected to be a new generation secondary battery.

Nanoscale metal oxides with different crystal structures have become one of the ideal anode materials for sodium-ion batteries due to their high energy density and long cycle life. Based on the abundant reserves and environmental friendliness, the application prospects of iron materials in sodium-ion batteries have been deeply studied. Fe_2O_3 has a high theoretical capacity (1007 $mAh\cdot g^{-1}$); however, similar to other metal oxides, it has to confront large volume expansion and poor conductivity [11-15]. Volume expansion can lead to poor structural stability and even collapse of the crystal structure. Poor conductivity leads to continuous SEI (solid electrolyte interface) formation, which eventually results in the continuous reduction of capacity in charging-discharging cycles.

To improve the electrochemical properties of Fe_2O_3 materials, researchers have committed to preparing novel micro/nanostructures and various nanocomposites to improve ion and electron transport and address the volume expansion problem. It has been reported that porous Fe_2O_3 nanotubes can provide much higher charging-discharging capacity than bare Fe_2O_3 nanoparticles [11, 16, 17]. Compared with nonporous microstructures, porous nanostructures can provide a larger surface area, which can ensure more contact between the electrolyte and electrode surface and further promote charge transfer between the electrode and electrolyte interface.

Therefore, the introduction of porous channels or matrix support systems into electrode materials is an important method to improve the cycle performance and rate performance of the batteries, which has become a very valuable research direction at this stage. In this research, Fe_2O_3-300@GF, Fe_2O_3-400@GF and Fe_2O_3-500@GF were prepared by calcination at 300 °C, 400 °C and 500 °C, respectively.

2. EXPERIMENTAL

2.1 Synthesis of α-FeOOH@GF nanorods

α-FeOOH@GF nanorod were obtained by a hydrothermal method. First, the 3D graphene foam was pretreated with nitric acid to remove the surface oxide layer. Then, 4 mmol $FeCl_3\cdot 6H_2O$ and 60 mmol urea were dissolved in 20 mL deionized water with magnetic stirring for 0.5 h. Afterwards, 1.5 mL of 37% hydrochloric acid was added to the above mixed solution and continuously stirred for 10 min to form a new uniform mixed solution. The mixed solution and 3D graphene foam were transferred to a 50 ml Teflon stainless steel autoclave and maintained in a hydrothermal reaction at 150 °C for 15 h. Finally, the samples were washed three times with deionized water and ethanol.

2.2 Synthesis of Fe_2O_3@GF

The α-FeOOH@GF precursor was calcinated with a heating rate of 2 $°C\cdot min^{-1}$ for 2 h at 300 °C, 400 °C and 500 °C. Calcination was carried out in an air atmosphere. The obtained products were labelled as Fe_2O_3-300@GF, Fe_2O_3-400@GF and Fe_2O_3-500@GF, respectively.

2.3 Electrochemical measurements

The electrochemical experiments were studied with coin cell (CR2032-type, half-cell) using Na foil as the counter electrode. Fe_2O_3@GF as self-supporting material, it can be directly punched into a circular plate with a diameter of 10mm as the working electrode. The battery was assembled in a glove box filled with inert gas. The voltage range for charging and discharging test was 0.01 V-3.0 V. The cyclic voltammetry curve (CV) and electrochemical impedance spectra (EIS) were measured by electrochemical workstation CHI660. All electrochemical properties were tested at room temperature.

3. RESULTS AND DISCUSSION

3.1 Microstructure of Fe_2O_3@GF

The effect of calcination temperature on the composition and structure of Fe_2O_3@GF was investigated by XRD, and the results are shown in Figure 1. Figure 1(a) shows the characteristic diffraction peaks observed correspond to the FeOOH phase (JCPDS No.:81-0462) without any other diffraction peaks. The XRD pattern of Fe_2O_3-400@GF obtained for the α-FeOOH@GF precursor calcined at 400 ℃ for 2 h is shown in Figure 1(b). As described in the figure, all the diffraction peaks can be calibrated by Fe_2O_3 (JCPDS No.: 87-1166), and no other obvious peaks were found in the diffraction pattern, indicating that iron hydroxide completely transformed into Fe_2O_3 after calcination in air. In addition, at a calcination temperature of 300 ℃, Fe_2O_3-300@GF contained not only a diffraction peak due to α-FeOOH precursor, but also a diffraction peak of Fe_2O_3. Therefore, iron hydroxide can be converted into Fe_2O_3 at approximately 400 ℃.

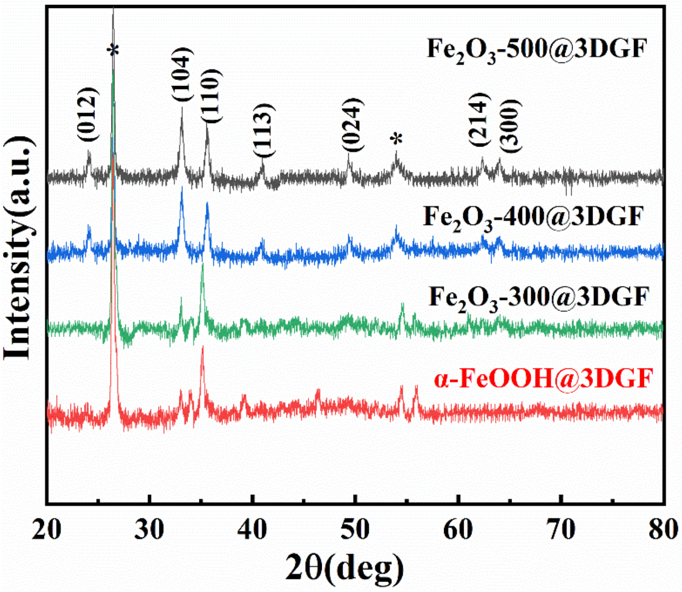

Figure 1. XRD patterns for α-FeOOH@GF and Fe_2O_3@GF

The chemical composition and valence state of Fe_2O_3-400@GF were further analyzed by X-ray photoelectron spectroscopy (XPS), as shown in Figure 2. Figure 2(a) shows the full spectrum of Fe_2O_3-300@GF, which proved the presence of Fe, O and C elements in the sample. Figure 2(b) shows the elemental spectrum of Fe 2p. The spectral peaks at 710.9 eV and 724.6 eV are the characteristic peaks for Fe $2p^{3/2}$ 和 Fe $2p^{1/2}$, respectively, similarity with findings of Yamashita [18]. At the same time, two satellite peaks were found around the main peaks, which confirmed the existence of Fe^{3+}. Figure 3(c) reveals the elemental spectrum of O 1s. The peaks at 529.9 eV and 531.7 eV might be the characteristic peaks of the O^{2-} and C-O bonds. Figure 4(d) shows the elemental spectrum for C 1s. The peak at 284.8 eV corresponded to the characteristic peaks of the carbon sp^2 bond (C-C), which indicates that the calcined residue was carbonized.

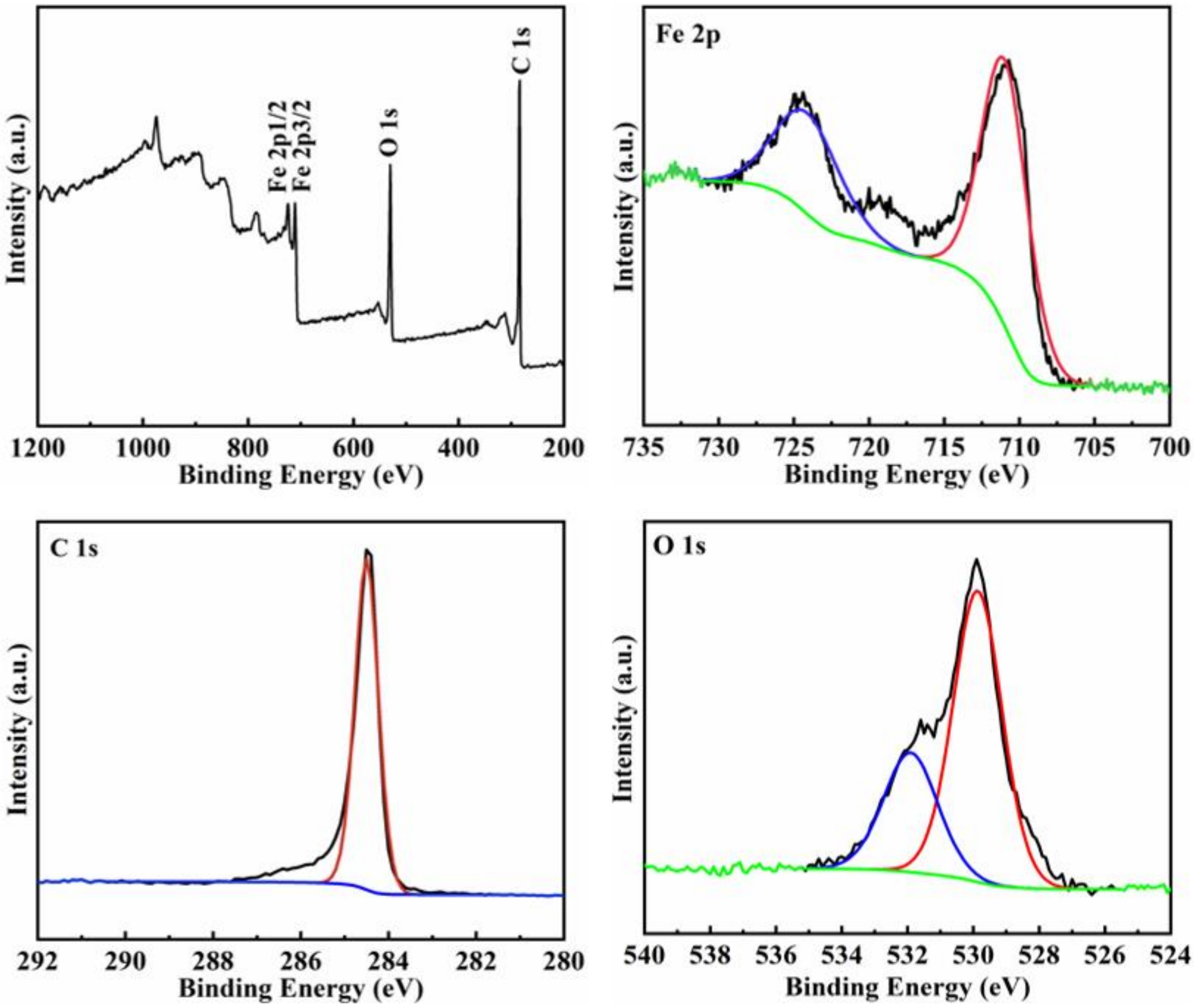

Figure 2. XPS spectra for Fe_2O_3-400@GF: (a) full spectra, (b) Fe 2p, (c) O 1s, (d) C 1s

Figure 3 reveals the morphology and characteristics for Fe_2O_3-300@GF、Fe_2O_3-400@GF and Fe_2O_3-500@GF. From all the SEM images for the three samples, the products showed similar typical rod structures regardless of calcination at 300 °C, 400 °C or 500 °C. Although the products were all rod-shaped structures, they were very different in detail. The size distribution of Fe_2O_3-300@GF was uniform, and the surface was smooth and even. This result is similar to that obtained for Fe_2O_3-400@GF, with a length of 90 nm-100 nm and height of 200 nm-250 nm. The Fe_2O_3-300@GF nanorods showed obvious agglomeration, and the length of the particles was relatively significant, as shown in Figure 3(e). Moreover, the SEM images of the three samples shown in Figure 3(b), Figure 3(d) and Figure 3(f) contained porous materials of different sizes on the surface of the nanorods. The pore size increased with increasing calcination temperature. There were many small holes distributed on the surface of Fe_2O_3-300@GF and Fe_2O_3-400@GF, but the hole size for Fe_2O_3-500@GF was the largest, which led to an unstable nanorod structure.

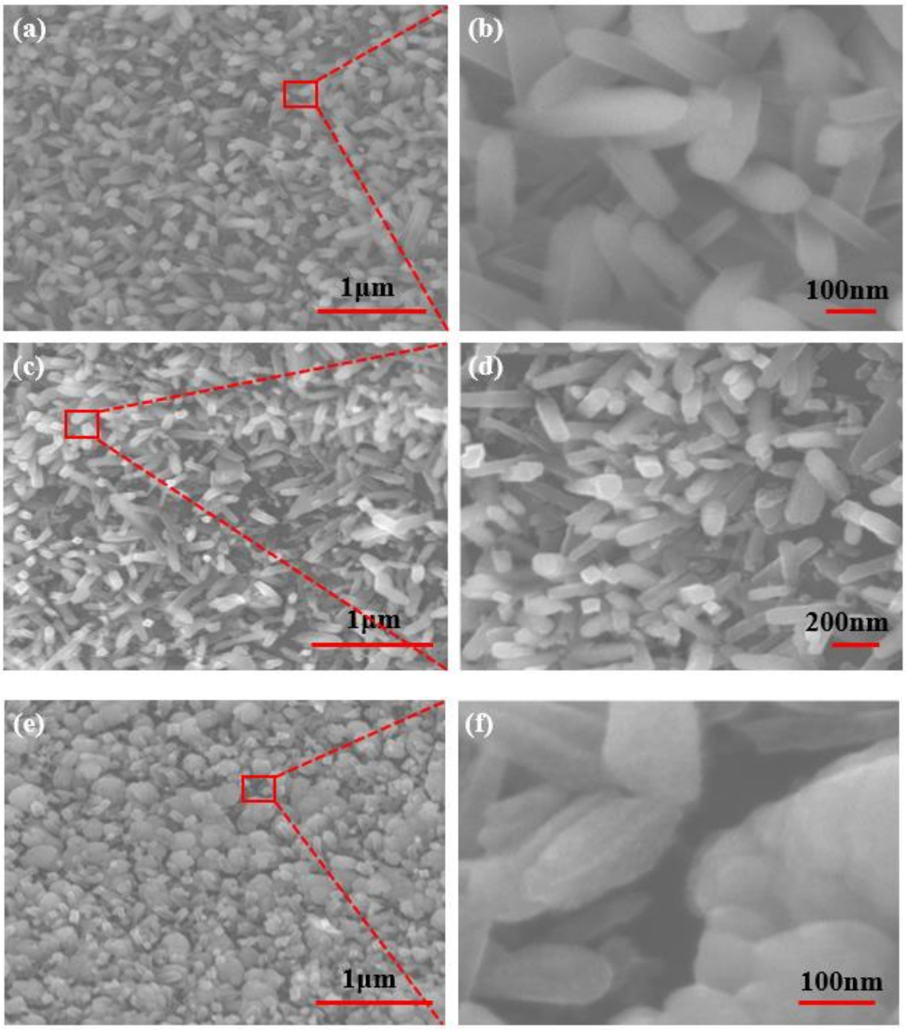

(a) Fe_2O_3-300@GF (b) amplification of Fe_2O_3-300@GF
(c) Fe_2O_3-400@GF (d) amplification of Fe_2O_3-400@GF
(e) Fe_2O_3-500@GF (f) amplification of Fe_2O_3-500@GF

Figure 3. SEM image of different materials

To further study the microstructure characteristics of Fe_2O_3-300@GF, Fe_2O_3-400@GF and Fe_2O_3-500@GF, TEM results are shown in Figure 4. From the TEM images of the three samples, holes are observed in the nanorods, with slightly different holes sized observed at different calcination temperatures. Figure 4(a) shows that the contrast image of Fe_2O_3-300@GF is clear, implying obvious porous structures between the calcined products and within the internal structure of the nanorods. Figure 4(b) shows a single nanorod image of Fe_2O_3-400@GF. It can be clearly seen from this figure that not only pores exist on the surface of the sample, but also a large number of cavities inside the nanorod.

With increasing calcination temperature, the pore size increased gradually. After the calcination temperature was increased to 500℃, the Fe_2O_3-500@GF nanorod structure was destroyed to a certain extent, leading to instability of the structure, which might affect the performance of subsequent electrochemical tests. There are two reasons for the formation of pores. One might be the recrystallization of the α-FeOOH@GF precursor during calcination. The other might be due to the loss of a large number of organic groups. Generally, a microstructure with more pores and a larger surface area is beneficial for the intercalation/removal of sodium ions and can effectively reduce the stress generated by volume changes [19-20]. In short, the α-FeOOH@GF precursor calcined at 400℃ can gain a larger pore volume and stable porous framework, which is more beneficial for improving the storage performance of sodium.

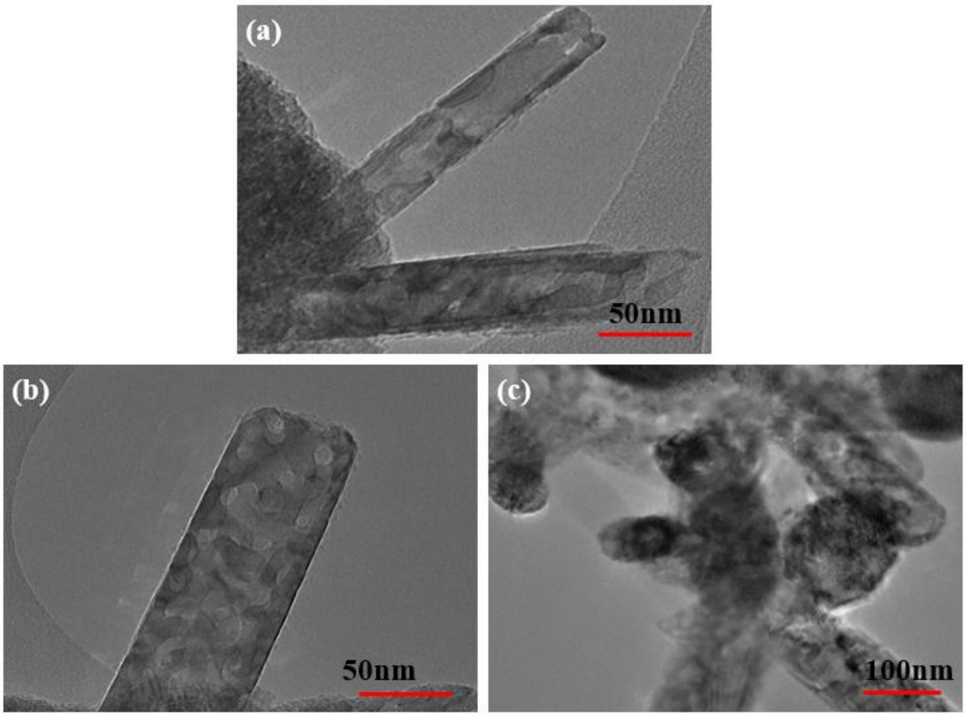

Figure 4. TEM image of three samples: (a) Fe_2O_3-300@GF, (b) Fe_2O_3-400@GF, (c) Fe_2O_3-500@GF

To further explore the pore size distribution and changes in pore size with calcination temperature for Fe_2O_3-300@GF, Fe_2O_3-400@GF and Fe_2O_3-500@GF, nitrogen adsorption/desorption isotherms were measured at 77 K, as shown in Figure 5. It can be seen from this figure that the isothermal adsorption/desorption curves for the three samples can be classified as type IV. A small hysteresis curve was observed under a relative pressure of 0.1~1, which is characteristic of mesoporous material adsorption/desorption. It was found that the BET surface area of Fe_2O_3-400@GF is higher than that of Fe_2O_3-300@GF and Fe_2O_3-500@GF. The higher surface area might be due to the small grain size and consistent with the porous structure observed in the TEM images. The porosity in these samples is attributed to the shrinkage of the GF layer and recrystallization during heat treatment.

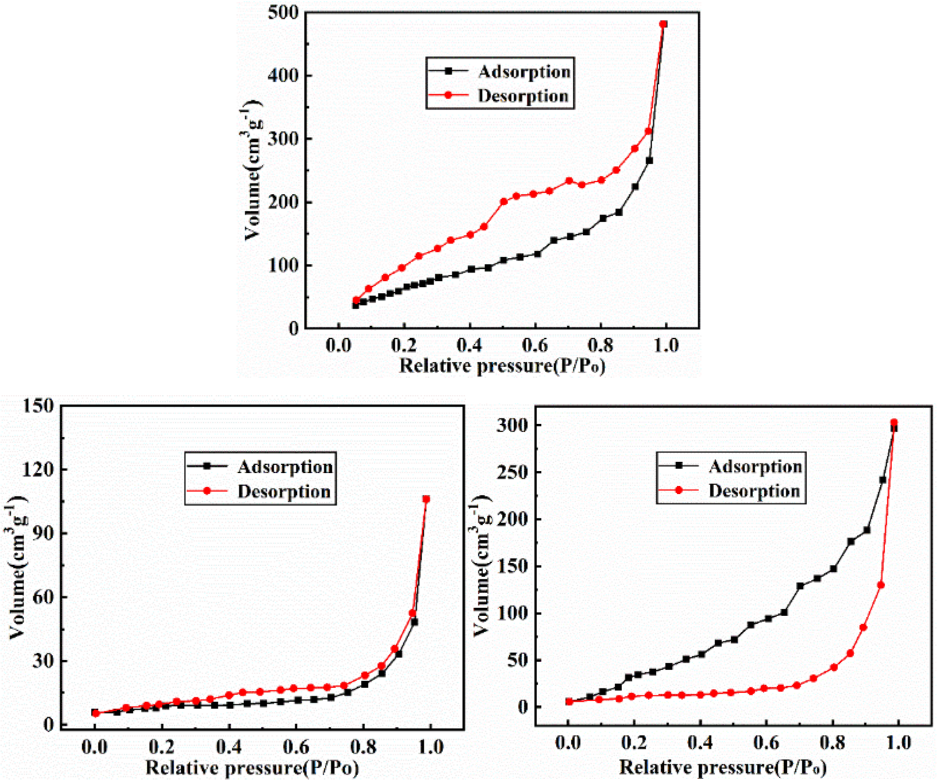

Figure 5. N_2 adsorption-desorption isotherms for samples: (a) Fe_2O_3-400@GF, (b) Fe_2O_3-300@GF, (c) Fe_2O_3-500@GF

3.2 Electrochemical characterization

Figure 6 depicts the cycling performance of Fe_2O_3-300@GF, Fe_2O_3-400@GF and Fe_2O_3-500@GF at a current density of 500 mA·g^{-1}. As shown in the figure, the first discharging capacity of Fe_2O_3-400@GF is 584 mAh·g^{-1}, and the first charging capacity of Fe_2O_3-400@GF is 562 mAh·g^{-1}, with coulombic efficiency of 96.2%. As the charging-discharging cycles increased, the capacity decreased continuously. When the number of cycles reached 10 cycles, the charging-discharging capacity achieved a stable state and remained at almost 200 cycles at 436 mAh·g^{-1}, which is 77.6% of the initial capacity. The cycling performance of Fe_2O_3-300@GF is similar to that of Fe_2O_3-400@GF. The coulombic efficiency was determined to be 95.8%, and the charging-discharging capacity decreased with increasing cycle number. The difference was that the charging-discharging capacity dramatically decreased after 100 cycles, which might be due to the collapse of the structure and termination of electron transport pathway. After that, the capacity was maintained at 251 mAh·g^{-1} until 200 cycles, which is 55.8% of the initial capacity. However, the cycling performance of Fe_2O_3-500@GF was found to be different from that of Fe_2O_3-300@GF and Fe_2O_3-400@GF. For example, during the first 50 cycles, the charging-discharging capacity gradually increased with increasing cycle number. The reason for this phenomenon might be due to the activation of the active materials. In detail, the structure of Fe_2O_3-500@GF might be rearranged, which is favourable towards irreversible Na_2O formed in the reaction re-participating in the electrochemical reaction. After 200 cycles, the capacity reached 288 mAh·g^{-1}, which is only 62.6% of the initial capacity.

Among the three samples, Fe_2O_3-400@GF showed the highest stable cycle performance, which might be related to the high content of graphene foam, which can buffer the volume expansion [21]. Therefore, the prepared Fe_2O_3-400@GF has potential applications in sodium-ion batteries.

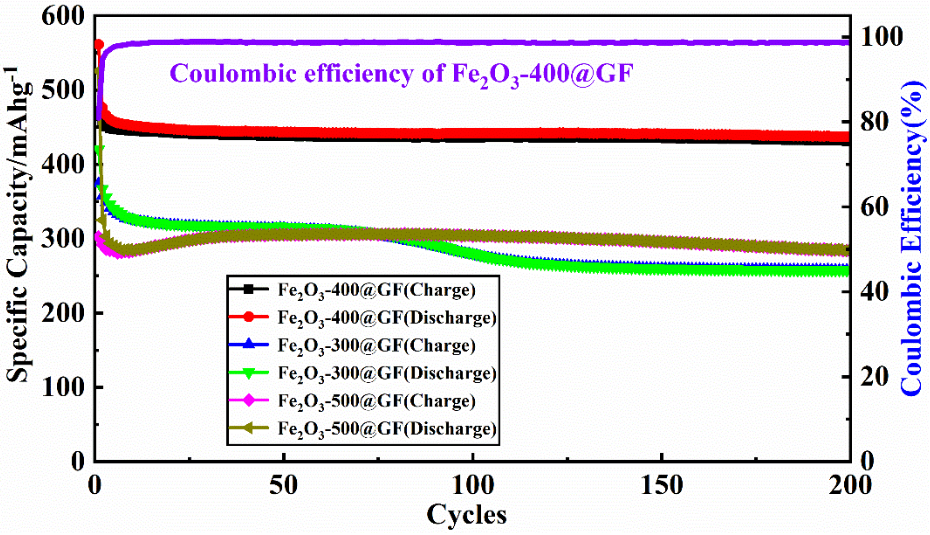

Figure 6. Cycling performance of Fe_2O_3-300@GF, Fe_2O_3-400@GF and Fe_2O_3-500@GF at a current of 500 mA·g^{-1}

Figure 7 shows the charging-discharging curves obtained for Fe_2O_3-400@GF at a current density of 500 mA·g^{-1} for the first cycle, 100th cycle and 200th cycle. Generally, the charging-discharging curve can be divided into two parts according to the type of chemical reaction. If the voltage is higher than 0.8 V, the conversion reaction mechanism is dominant, and if the voltage is lower than 0.8 V, the surface adsorption reaction mechanism is dominant. The capacity of Fe_2O_3-400@GF provided by the conversion reaction mechanism was found to be stable during the whole charging-discharging cycle, while the capacity provided by the surface adsorption reaction mechanism gradually increased. The first charging-discharging curve was completely different from that of the next 100th and 200th cycles because the irreversible capacity loss is mainly due to irreversible side reactions on the electrode surface, such as the formation of an SEI layer and the decomposition and consumption of electrolyte [22-24]. There was almost no difference found between the charging-discharging curves for the 100th and 200th cycles. This indicates that the Fe_2O_3-400@GF structure is very stable during cycling, which is consistent with the research results shown in Figure 6.

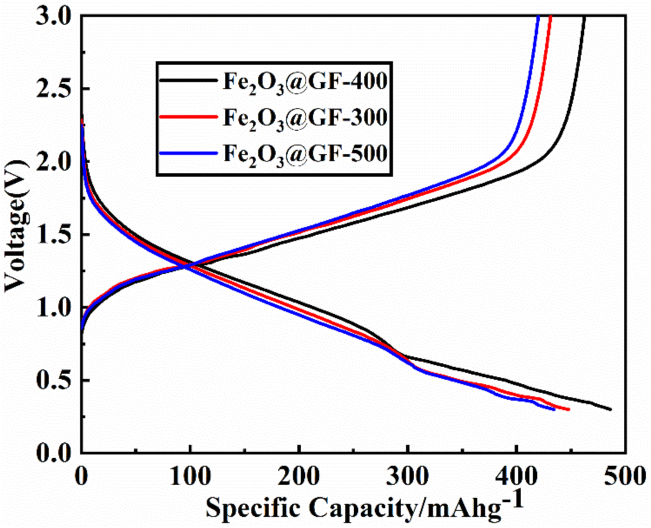

Figure 7. Charge-discharge curves for Fe_2O_3-400@GF at different cycles

Figure 8 shows the rate performance of Fe_2O_3-300@GF, Fe_2O_3-400@GF and Fe_2O_3-500@GF at different current densities (0.1 A·g^{-1} to 2.0 A·g^{-1}). It can be seen from the figure that the charging-discharging capacity of Fe_2O_3-400@GF is higher than that of Fe_2O_3-300@GF and Fe_2O_3-500@GF, showing good stability and high specific capacity. In addition, when the current density returns to the initial current density of 0.1 A·g^{-1}, the charging-discharging capacity of the three materials can be restored to a higher degree, and is only slightly lower than the initial capacity. The above results show that the three materials all have good rate performance, but the rate performance of Fe_2O_3-400@GF is better than that of Fe_2O_3-300@GF and Fe_2O_3-500@GF. The high reversible capacity of the three electrode materials can be attributed to their unique nanorod structure and close combination with the three-dimensional graphene foam. The coupling effect between them can provide more active centres for Na^+ intercalation and improve the utilization of active materials. Additionally, the results of this paper were compared with the results of the existing literature, as shown in Table 1. Table 1 showed that the Fe_2O_3-400@GF has good cycle stability and rate performance.

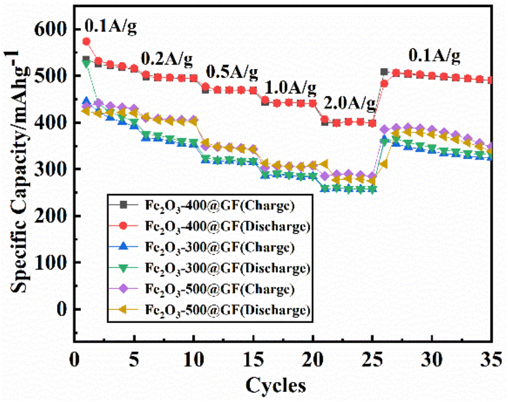

Figure 8. Rate capacity at different rates for Fe_2O_3-300@GF、Fe_2O_3-400@GF and Fe_2O_3-500@GF at different current densities (0.1 A·g^{-1}-2.0 A·g^{-1})

Table 1. Recent progress on material synthesis and electrochemical performance of Fe_2O_3-400@GF batteries

Materials	Voltage range (V vs Na^+/Na)	Cycling data	Rate capability	Ref.
porous Fe_2O_3@C	0.01-3.0	203/100th/200 $mA\cdot g^{-1}$	64/4 $A\cdot g^{-1}$	**[11]**
γ-Fe_2O_3	0.01-3.0	198.2/80th/475 $mA\cdot g^{-1}$	-	**[16]**
α -Fe_2O_3	0.01-3.0	78.3/80th/475 $mA\cdot g^{-1}$	-$^{-1}$	**[16]**
Fe_2O_3-400@GF	0.01-3.0	436/200th/500 $mA\cdot g^{-1}$	398/2 $A\cdot g^{-1}$	This paper

To further study the difference in sodium storage performance for the three kinds of samples, the electrochemical impedances of Fe_2O_3-300@GF, Fe_2O_3-400@GF and Fe_2O_3-500@GF were measured. Figure 9 shows the electrochemical impedance curve obtained for the three samples after 200 charging-discharging cycles. It can be clearly seen that the electrochemical impedance curves for the three electrode materials show semicircles in the high frequency region, microsemicircles in the medium frequency region and nearly straight lines in the low frequency region [25-26]. According to calculation, the charge transfer resistance (RCT) for Fe_2O_3-400@GF is 22.7 Ω, which is smaller than that of Fe_2O_3-300@GF and Fe_2O_3-500@GF by 32.4 Ω and 42.6 Ω, respectively. This calculation indicates that Fe_2O_3-400@GF has a relatively high conductivity, which is very helpful to improve the sodium storage capacity at a high rate.

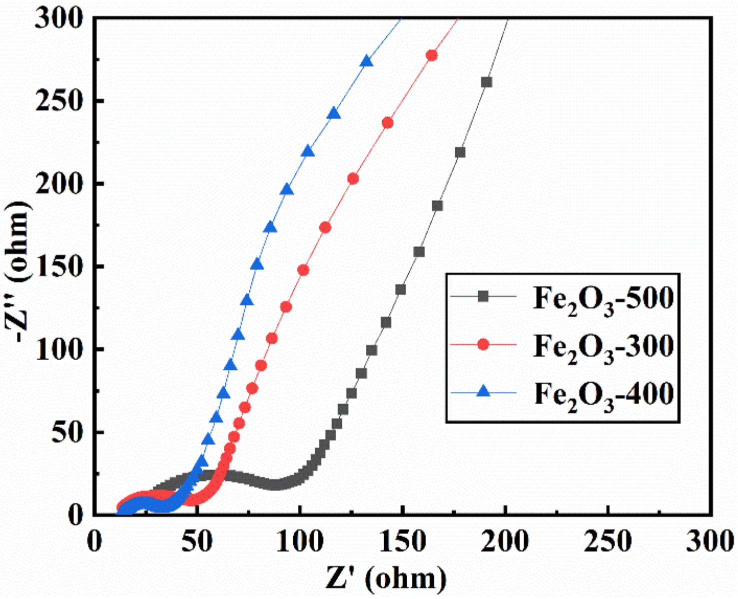

Figure 9. Electrochemical impedance spectra (EIS) for Fe_2O_3-300@GF, Fe_2O_3-400@GF and Fe_2O_3-500@GF after 200 cycles

4. CONCLUSION

This paper successfully synthesized controllable Fe_2O_3-300@GF, Fe_2O_3-400@GF and Fe_2O_3-500@GF composites through calcination at different temperatures. Compared with electrode materials calcined at 300°C and 500 °C, Fe_2O_3-400@GF calcined at 400°C showed good cycle stability and high-rate performance, with a retention capacity of 410 $mAh \cdot g^{-1}$ at 2 $A \cdot g^{-1}$.

The improvement in the sodium storage performance of Fe_2O_3-400@GF was due to a reasonable particle size distribution and good structural stability. Meanwhile, the three-dimensional graphene foam was helpful for the structural stability during charging-discharging cycles, which can provide more activity points for Na^+ insertion. On the other hand, Fe_2O_3-400@GF with an appropriate pore size and large surface area can promote ion transport and buffer the stress generated by volume change, which can effectively reduce the volume expansion problem and improve the cycle stability and rate performance of the electrode.

ACKNOWLEDGEMENTS
National Natural Science Foundation of China (51804091)

References

1. J. Bai, H. Wu, S. Wang, G. Zhang, *J. Electron Mater.*, 48 (2019)5933.
2. L. Zhou, K. Zhang, Z. Hu, Z. Tao, L. Mai, Y.M. Kang, S.L. Chou, J. Chen, *Adv. Energy Mater.*, 6 (2018)1.
3. Y.J. Zhang, W. Chang, J. Qu, S.M. Hao, Q.Y. Ji, Z.G. Jiang, Z.Z. Yu, *Chem-Eur J.*, 65 (2018) 17339.
4. Y. Zhang, N. Wang, C. Sun, Z. Lu, P. Xue, B. Tang, Z. Bai, S. Dou, *Chem. Eng. J.*, 332 (2018) 370.
5. C. Zhang, Y. Xu, W. Chen, L. Sun, D. Xu, Y. Yan, X. Yu, *J. Electroanal. Chem.*, 816 (2018) 114.
6. S. Yu, V. Ng, F. Wang, Z. Xiao, C. Li, L.B. Kong, W. Que, K. Zhou, *J. Mater. Chem. A*, 20 (2018) 9332.
7. J. Yuan, W. Liu, X. Zhang, Y. Zhang, *J. Power Sources,* 455 (2020) 227937.
8. L. Yao, W. Xia, H. Zhang, H. Dong, H.L. Xin, *Nano Energy*, 60 (2019) 424.
9. S. Yang, G. Shao, Z. Hao, *Adv. Energy Mater.*, 23 (2019) 1.
10. Y. Wang, W. Lai, Y. Wang, Y. X. Cao, S. Chou, *Angew. Chem.Int. Edit.*, 51(2019) 58.
11. B. Wang, S. Zhang, G. Wang, H. Wang, J. Bai, *J. Colloid Interface Sci.*, 557 (2019) 216.
12. Y. Sun, S. Guo, H. Zhou, *Adv. Energy Mater.*, 23(2019) 1.
13. S. Qi, L. Mi, K. Song, K. Yang, J. Ma, X. Feng, J. Zhang, *The Journal of Physical Chemistry C*, 123 (2019) 2775.
14. X. Pu, H. Wang, D. Zhao, H. Yang, X. Ai, *Small*, 1(2019) 1805427.
15. J.K. Kim, S.K. Park, J.S. Park, Y.C. Kang, *J. Mater. Chem. A*, 6 (2019) 2636.
16. D. Nayak, S. Puravanka, S. Ghosh, V. Adyam, *Ionics*, 25 (2019) 5857.
17. Y. Su, B. Fu, G. Yuan, M. Ma, *Nanotechnology*, 15(2019) 31.
18. T. Yamashita, P. Hayes. *Appl. Surf. Sci*, 254(2008):2441.
19. X. Wang, Q. Xiang, B. Liu, L. Wang, T. Luo, D. Chen, G. Shen, *Sci. Rep*, 3(2013) 2007.
20. T. Jiang, F. Bu, X. Feng, I. Shakir, G. Hao. *ACS Nano*, 11(2017) 5140.
21. X. Chai, C. Shi, E. Liu, J. Li, N. Zhao, C. He. *Appl. Surf. Sci*, 347(2015) 178.
22. S.B. Ranganath, A.S.Hassan, B. R. Ramachandran, *J. Electrochem. Soc*, 163(2016) 2172.
23. J. W. Wen, D. W. Zhang, Y. Zang, X. Sun. *Electrochim. Acta*, 132(2014) 193.

24. Y. Zhang, P.H. Chen, X. Gao, B. Wang, H. Liu, H. Wu, H.K. Liu, S.X. Dou, *Adv. Funct. Mater*, 26 (2016) 7754.
25. T. Xia, W. Zhang, J. Mur, G. Liu, X. Chen. *Nano Lett.*, 13(2013) 5289.
26. T. Li, Y. Wang, R. Tang, Y. Qi, N. Lun, Y. Bai, R. Fan. *ACS Appl. Mater., Interfaces*, 5(2013) 9470.